Nonuniform flow in soft glasses of colloidal rods

J. K. G. Dhont*

Forschungszentrum Jülich, Institute of Complex Systems (ICS-3), D-52425 Jülich, Germany
and Heinrich-Heine Universität Düsseldorf, Department of Physics, D-40225 Düsseldorf, Germany

K. Kang and H. Kriegs

Forschungszentrum Jülich, Institute of Complex Systems (ICS-3), D-52425 Jülich, Germany

O. Danko

Taras Shevchenko National University Kyiv, Kyiv, Ukraine

J. Marakis and D. Vlassopoulos

Foundation for Research and Technology–Hellas (FORTH),
Institute of Electronic Structure and Laser (IESL), GR-70013 Crete, Greece
and University of Crete, Department of Materials Science and Technology, GR-71003 Crete, Greece

Despite our reasonably advanced understanding of the dynamics and flow of glasses made of spherical colloids, the role of shape, i.e., the respective behavior of glasses formed by rodlike, particles is virtually unexplored. Recently, long, thin and highly charged rods (fd-virus particles) were found to vitrify in aqueous suspensions at low ionic strength [Phys. Rev. Lett. **110**, 015901 (2013)]. The glass transition of these long-ranged repulsive rods occurs at a concentration far above the isotropic-nematic coexistence region and is characterized by the unique arrest of both the dynamics of domains that constitute the chiral-nematic orientational texture, as well as individual rods inside the domains. Hence, two relevant length scales exist: the domain size of a few hundreds of microns, and the rod-cage size of a few microns, inside the domains. We show that the unique dual dynamic arrest and the existing of two widely separated length scales imparts an unprecedented, highly heterogeneous flow behavior with three distinct signatures. Beyond a weak stress plateau at very small shear rates that characterizes the glass, the kinetic arrest of the domain dynamics gives rise to internal fracture, as a result of domain-domain interactions, as well as wall partial slip. It is shown that, on increasing the shear rate, the fractured plug flow changes to a shear-banded flow profile due to the stress response of the kinetically arrested aligned rods within the domains. Shear-gradient banding occurs due to the strong thinning of the uniform chiral-nematic phase within the domains, i.e., complying with the classic shear-banding scenario, giving rise to a stress plateau in the flow curve. Finally, a linear (uniform) velocity profile is found at the highest shear rates. Vorticity banding is also observed at intermediate and high shear rates. These results point to the crucial role of particle shape in tailoring the flow properties of dense colloidal suspensions. Moreover, they strongly support the argument that the origin of shear banding in soft-particle glasses with long-ranged repulsive interactions is fundamentally different from that of hard-particle glasses with short-ranged repulsive interactions.

I. INTRODUCTION

Many types of materials, ranging from colloids to polymers and metals, exhibit a glass transition, where a fluid-like disordered structure is dynamically arrested upon increasing packing fraction and/or changing the temperature. In a colloidal glass of repulsive particles, each particle is surrounded by an assembly of neighbors which prevent it from moving over distances larger than the typical

neighbor distance. At long time scales compared to the experimental, the particle is thus confined to an effective cage resulting from *repulsive* interactions with its neighbors; this is the so-called "caging." Glasses should be distinguished from gels, which are also long-lived nonequilibrium states, resulting, however, from *attractive* interactions. Long-lived nonequilibrium states often reflect an interplay of repulsive and attractive forces [1,2].

There is large body of literature on glasses of colloidal suspensions of *spheres*, with repulsive interparticle interactions ranging from short-ranged (hard spheres) to long-ranged (soft spheres). These systems have been used to gain fundamental understanding of the physics of glasses (an overview on such colloidal glasses can be found in Ref. [3]). There is only very little recent evidence on the behavior of glasses of *slightly anisotropic* colloidal particles [4–6]. In particular, such glasses have been found to exhibit "double yielding" as evidenced by a double maximum in the frequency dependence of the viscous modulus. The double yielding (originally reported for attractive glasses from colloid-polymer mixtures [7]) has been attributed to the respective onset of rotational and translational motion. Two peaks in the viscous modulus were also observed in glasses of core-shell colloids with attractive forces for very different reasons: the peaks are attributed to the deformation of the shell and cage breaking, respectively [8]. Similarly, soft glasses of interpenetrating star polymers were also reported to exhibit two-step yielding at high enough frequencies before complete disengagement [9].

Depending on the applied shear rate, colloidal glasses of spherical particles may exhibit inhomogeneous flow profiles consisting of two bands, i.e., two regions extending along the gradient direction with distinct shear rates (overviews of shear-banding transitions in various types of systems can be found in Refs. [10–16]). For soft glasses of star polymers the "classic shear-banding instability" scenario suggests that strong shear thinning is responsible for the occurrence of nonuniform flow [17–21]. Such a strong shear thinning is also at the origin of shear banding in many different types of colloidal fluids, such as wormlike micellar solutions, lyotropic lamellar phases, solutions and blends of various types of polymers, polycrystalline colloids, and dispersions of platelets [10–16,22–26]. For glasses of particles with soft interactions, a number of intriguing features associated with the interplay of aging and shear banding have been described by the "soft glassy rheology" model [27–29] or the empirical "fluidity" model [18]. However, the exact role of microstructural details such as star interpenetration is not fully understood yet. Shear banding is also found for other types of systems with a yield stress such as gels [30,31], cement pastes [32], and emulsions [33–35]. Reference [36] gives an overview of various types of yield-stress systems, with a physical interpretation of the origin of banding scenarios for systems with attractive and repulsive interparticle interactions. The shear-banding scenario for hard-sphere glasses is fundamentally different from the classic banding scenario exhibited by the above mentioned soft star-polymer glasses at relatively low concentrations. For hard-sphere glasses an instability occurs due to mass transport induced by spatial gradients in the shear rate [37,38], the so-called Shear-gradient Concentration Coupling (SCC) instability, where one shear-band is strictly nonflowing. This instability is possibly also at the origin of the banded flow profiles found in molecular dynamics simulations of short-ranged repulsive particles in Ref. [39]. The reason for this fundamentally different shear-banding behavior of glasses consisting of particles with long- and short-ranged repulsive interactions will be discussed in more detail later.

Concerning purely repulsive *glasses of rodlike colloids* with large aspect ratio, two experimental systems have been reported: aqueous suspensions of boehmite rods [40] and fd-virus particles [41,42] at very low ionic strengths. The low ionic strengths correspond to large Debye lengths, thus resulting in long-ranged electrostatic repulsive interactions. These interactions are responsible for caging. In both cases, a glass transition far above the isotropic-nematic coexistence region was reported. Contrary to glasses of spheres, the morphology here consists of chiral-nematic domains with different orientations, which we shall refer to as "orientational texture." In Refs. [41,42] it is also shown that the dynamics of the orientational texture freezes at the same concentration where rodlike particle arrest is observed. There are thus two dynamical processes that are frozen at the same concentration: the particle dynamics and the dynamics of the orientational texture. These two processes involve two

length scales: the size of the cage due to long-ranged electrostatic interactions, of which the largest dimension is of the order of a few times the rod length (a few microns), and the size of chiral-nematic domains (several hundreds of microns). The existence of such widely separated length scales will be shown to lead to quite a different flow behavior as compared to glasses of spherical colloids. A practical overview addressing gels and glasses of anisotropic colloids can be found in Ref. [1]. Many of the systems that are referred to as glasses of rods in Ref. [1] are in fact systems where attractive interactions play an important role. Here we consider glasses of charged rods, with purely repulsive interactions due to the presence of thick electric-double layers, which lead to long relaxation times of collective dynamics [42].

The flow behavior of glasses of *rodlike* particles is unexplored, yet it is expected to give rise to new phenomena as compared to glasses of spherical particles due to the above mentioned existence of the two widely separated length scales associated with the cage size and the size of chiral-nematic domains. The purpose of this study is twofold: (1) to explore the complex flow and rheology of suspensions of rodlike colloids with long-ranged repulsive interactions near the glass transition, and decouple the contributions from the chiral-nematic orientational texture and the chiral-nematic phase within single domains and (2) to distinguish the two fundamentally different shear-banding mechanisms that lead to shear banding of glasses with long-ranged and short-ranged interparticle interactions.

As a model system for rodlike colloids, we use fd-virus particles, which consist of a double-stranded DNA covered with 2700 coat proteins. The contour length is 880 nm, the width of the fd-core is 6.8 nm, while the coat proteins render the fd-virus stiff, with a persistence length of about 2500 nm. This model system has been used to study the equilibrium phase behavior of charged colloidal rods at ionic strengths larger than about 1 mM (see, for example, Refs. [43–48]). For these quasi-hard-rod systems, a number of liquid-crystalline phases have been observed: a chiral nematic phase (where the rods have a preferred orientation, like in a nematic phase, but where the direction of the preferred orientation varies periodically), a smectic phase (which consists of stacked nematic layers), a columnar phase (where the rods are assembled in columns), and a crystalline phase. At these relatively high ionic strengths, no glass transition has been observed. A glass is found in Refs. [41,42] at a much lower ionic strength of 0.16 mM of TRIS/HCl buffer. In the present study we use the same low ionic strength, corresponding to a Debye length of 27 nm. The effective aspect ratio of the fd-rods is 33, quite different from the aspect ratio of 133 at high ionic strengths. The resulting long-ranged repulsive interactions between rods lead to particle arrest. Soft glasses with such long-ranged electrostatic interactions are commonly referred to as Wigner glasses (after E. Wigner, who predicted a crystal ordering of electrons as a result of their electrostatic interactions [49]). At higher ionic strengths (larger than about 0.5 mM) no glass state is observed, as the electrostatic interactions are not sufficiently long-ranged to form cages. For example, PNIPAM-coated fd-virus particles at relatively high ionic strengths do not form repulsive glasses [50,51]. Instead, these systems form a gel as the temperature is raised due to the attractive interactions between the polymer coatings. The possibility for inhomogeneous flow profiles for such gels of very long and thin attractive rods has so far not been studied. Here, however, we focus our attention on the above described soft repulsive glasses.

II. VISUAL OBSERVATION OF THE ORIENTIONAL TEXTURE UNDER FLOW

In order to interpret the origin of the various flow regimes discussed below, it is necessary to know to which extent the orientational nematic texture morphology is affected by flow. The experimental setup for imaging the orientational texture under flow conditions is sketched in Fig. 1 (the setup is combined with the light scattering apparatus to measure velocity profiles, as discussed in the next section). The gray area is the sample that is contained in an optical Couette cell, with smooth walls, of which the inner cylinder is rotated to induce shear flow. The gap width of the Couette cell is 1 mm and contains about 6.0 ml sample. The vertical optical train depicted in Fig. 1 is used for imaging of the domain morphology. The Couette cell is placed between two crossed polarizers A and P, and the transmitted intensity of the homogeneously illuminated cell with white light is recorded by a CCD camera using the 1:1 telescopic lens L3 in Fig. 1. The field-of-view is circular with a diameter of
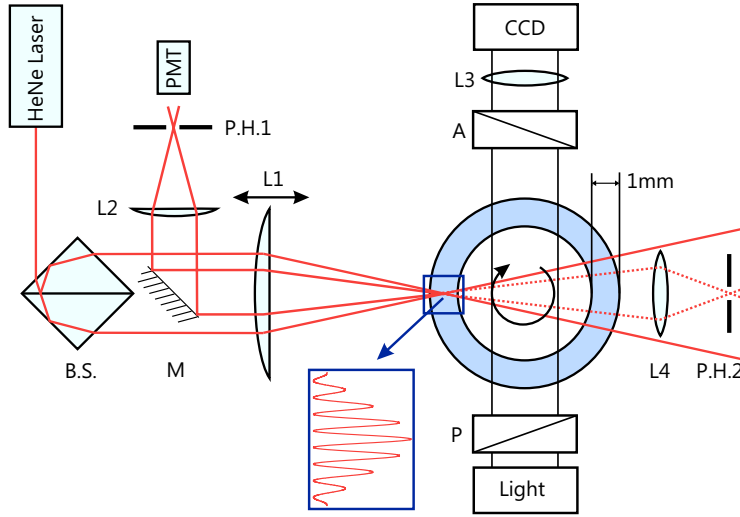
FIG. 1. Experimental setup for imaging *in situ* orientational textures under shear flow (the vertical optical train) and for laser Doppler heterodyne light scattering for the measurement of velocity profiles along the gradient direction (the horizontal optical train). The inset depicts the standing interference pattern within the region where two focused laser beams cross. Two scattering geometries are used, one for forward scattering and one for backward scattering.

3 cm. The images given in Fig. 2(a) show this circular field-of-view, while those in Fig. 2(b) are a rectangular part of it. The flow direction in these images is the horizontal direction, while the vertical direction is along the vorticity direction.

Since the fd-virus particles are birefringent, local orientational nematic order is evidenced by a nonzero transmitted intensity. The different colors in Fig. 2 are due to the wavelength dependence of the degree of birefringence of the fd-particles. The change in the polarization direction of the incident light thus depends on the wavelength, so that different colors are transmitted depending on the orientation of the domains.

The typical size of a chiral-nematic domain is 100–300 μm, while there are no strong anchoring conditions, so that for the gap width used here the morphology is essentially unaffected by confinement. Figure 2(a) shows full-view images for two shear rates and various concentrations (the field-of-view is 3 cm). The images of the orientational texture do not change over time spans of several days, so that these images represent stationary states. The encircled far-right images (in red) refer to a concentration that is above the glass transition. The lowest concentration (3.7 mg/ml) is just above the isotropic-nematic coexistence region. For a relatively low shear rate of $10\,\mathrm{s}^{-1}$ [the images in the lower panel in Fig. 2(a)], the bright regions correspond to single chiral-nematic domains. For the lowest concentration, the orientational texture is fully aligned at a shear rate of $50\,\mathrm{s}^{-1}$, resulting in the dark image in the most left upper image: the orientation of the rods is now along the polarization direction of one of the polarizers, so that no intensity is transmitted. Regular and thin, well-defined stripes are observed for the concentration of 7.4 mg/ml, well below the glass transition, while a much coarser banded morphology is observed very close and well above the glass transition [see the two images on the right, upper panel, in Fig. 2(a)]. For the two concentrations in the vicinity and within the glass (the glass transition concentration is 11.7 mg/ml [41,42]), single domains are present, contrary to the samples well below the glass transition.

Figure 2(b) shows a more detailed view of the orientational texture as function of shear rate for the same two high fd-concentrations as in Fig. 2(a), one just below the glass transition and one above the glass transition. The most left images of unsheared suspensions are the orientational textures as observed two days after filling the shear cell. For the higher concentration the originally
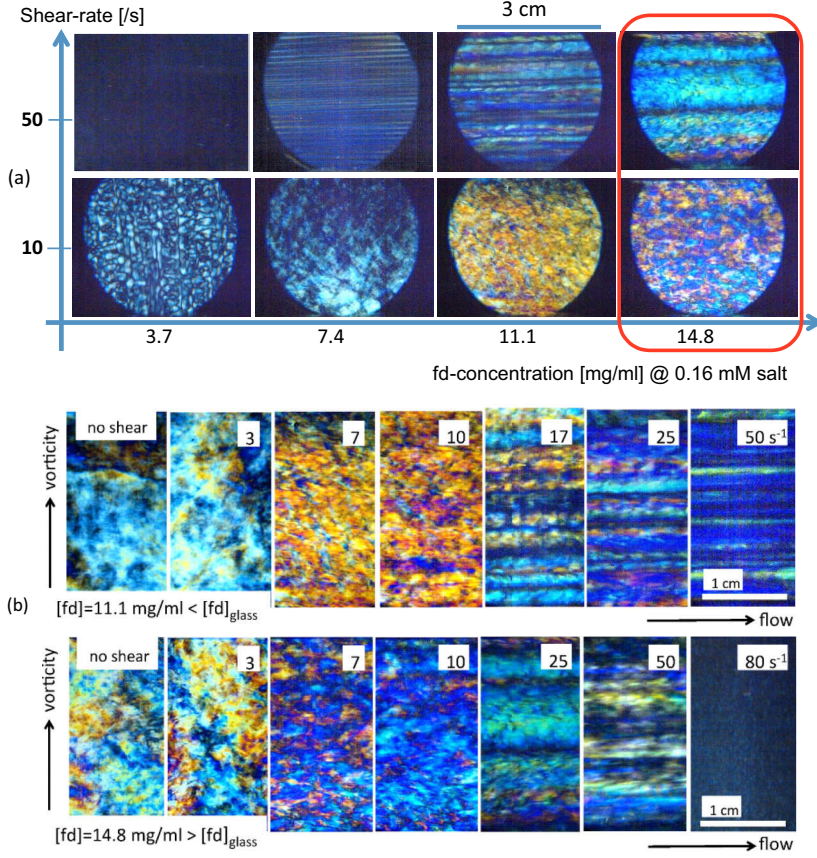
FIG. 2. Depolarized images of shear-affected chiral-nematic orientational texture. (a) A full view of the images of the texture for two shear rates, 10 and $50\,\mathrm{s}^{-1}$, for various concentrations as indicated in the figures. The diameter of the full-view images is 3 cm. The encircled far-right images (in red) refer to a concentration that is above the glass transition. (b) Images for a concentration of 11.1 mg/ml (upper panel), just below the glass transition, and for 14.8 mg/ml (lower panel) above the glass transition, for various shear rates as indicated in the different images. These images are cuts from the full-view images as given in (a).

shear-aligned texture, directly after filling the shear cell, does not change during two days, while for the lower concentration equilibration takes place (which is quantified through image-time correlation, as discussed in Refs. [41,42]). The morphology is not notably affected up to shear rates of a few reciprocal seconds. Vorticity bands develop at a shear rate of about $15\,\mathrm{s}^{-1}$ for both concentrations. The relatively blurry and much wider bands for the concentration above the glass transition are attributed to the fact that the domains are frozen in the glassy state, while for the lower concentration the domains are fluid-like.

There are several mechanisms that lead to different types of vorticity-banded morphologies. The classic Taylor instability is triggered by centrifugal forces, and leads to bands that are in internal rolling flow which span the gap of the Couette cell [as sketched in Fig. 3(h)]. The Taylor number $\mathrm{Ta} = \Omega^2\, R_1\, (R_2 - R_1)^3/\nu^2$ where vorticity banding sets in is of the order of 50, which is much lower than its critical value 3400 where a Newtonian fluid develops vorticity bands in a narrow-gap Couette cell (here Ω is the rotation velocity of the inner cylinder, R_1 is the outer radius of the inner cylinder, R_2 is the inner radius of the outer cylinder, and ν is the kinematic viscosity) [52–54]. Provided that the banded morphology is related to Taylor banding, this indicates that elastic deformation of the domains enhances the formation of Taylor vorticity bands [53–55]. Second, vorticity banding
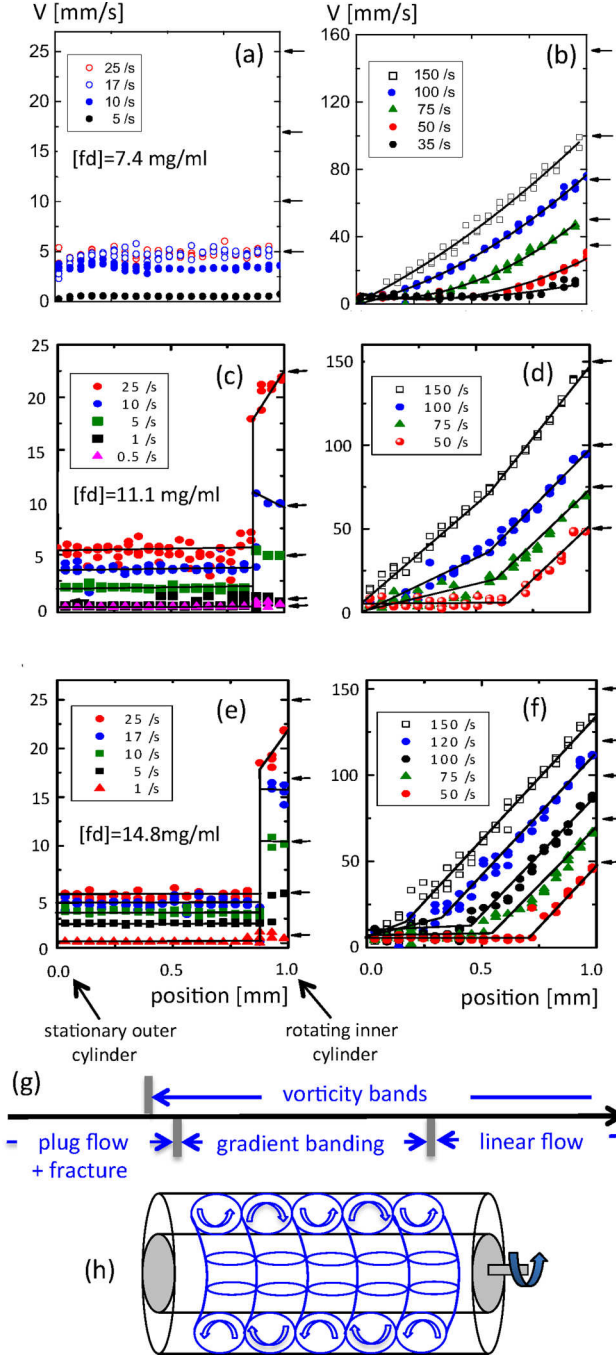
FIG. 3. Velocity profiles along the gradient direction for the same concentrations 7.4, 11.1, and 14.8 mg/ml as in Fig. 2, well below (a), (b), just below (c), (d), and above (e), (f) the glass transition, for various shear rates. The left-pointing arrows on the right axes indicate the velocities that correspond to no-slip conditions. The solid lines in (b) are fits to a second order polynomial and are guides-to-the-eye for the profiles in (c)–(f). The shear rate regimes where the different types of nonuniform flow are observed for the higher concentrations are sketched in (g). (h) A sketch of rolling flow in a Couette cell. The direction of the shear flow is perpendicular to the rolling flow, along the direction of the rotating inner cylinder.

can result from a purely elastic instability [56,57] or from a transient gradient-banded state where the interface between the gradient bands becomes unstable [55,58]. Like for Taylor banding, these mechanisms lead to vorticity bands that are in internal rolling flow, which span the entire gap of the Couette cell. Third, nematic domains may be stretched and merge to an extent that they span the circumference of the Couette cell. This is probably the mechanism leading to the thin bands for the low concentration of 7.4 mg/ml in Fig. 2(a). Observation of the time-dependent orientational texture under flow conditions reveal that the rolling flow velocity within the vorticity bands, in the vicinity and above the glass transition, is very much smaller as compared to the applied shear flow velocity [59].

An important conclusion from the above observations is that, for concentrations close to and above the glass concentration, the orientational texture is still present up to quite high shear rates, even within the shear-rate range where vorticity banding occurs, and that the velocity of a possibly present rolling flow within the bands is very much smaller than the applied shear flow velocity. As will be seen later, the presence of the orientational texture is at the origin of internal fracture, while the uniform chiral-nematic material within domains is responsible for gradient shear banding.

Banded structures stacked along the vorticity direction and aligned along the flow direction were observed and predicted in liquid-crystalline polymers (see, for example, Refs. [60–69], where in the latter reference fd-virus suspensions are investigated). In some of these studies transient bands have been observed that orient along the vorticity direction upon cessation of the flow. These phenomena are also observed in our experimental system of chiral-nematic fd-virus suspensions at low concentrations, below the glass transition, where the vorticity bands are quite regular [like those in Fig. 2(a) for an fd-concentration of 7.4 mg/ml at a shear rate of $50\,\mathrm{s}^{-1}$].

The present study focuses on the flow behavior of glassy suspensions, whereas a detailed analysis of the behavior of the orientational texture will be presented in future work.

III. INTERNAL FRACTURE, PLUG FLOW, AND SHEAR-GRADIENT BANDING

Velocity profiles along the gradient direction are obtained by spatially resolved heterodyne light scattering, using either a back-scattering or forward-scattering configuration. As sketched in Fig. 1, two parallel He-Ne laser beams with a wavelength of 633 nm are focused by the lens L1 at the same point within the gap of an optical Couette cell (the same cell, with smooth walls, as used in the previous section to record images of the nematic morphology), by which a standing interference pattern with a spacing of $1.46\,\mu$m is created, which corresponds to a grating wave vector of $4.36 \times 10^{6}\,\mathrm{m}^{-1}$. The angle between the two laser beams is $25°$, so that the scattering wave vector q for a single beam in the back-scattering direction is equal to $2.78 \times 10^{7}\,\mathrm{m}^{-1}$. The back-scattering detection path uses also the lens L1, which makes this configuration more stable compared with the detection in forward direction (see the dotted lines in Fig. 1). For the forward-scattering configuration, the scattering wave vector is about a factor of 10 smaller as compared to the back-scattering configuration. Therefore the diffusion dependent time constant in the correlation function is about two orders of magnitude slower in the forward-scattering configuration and can provide a feasible signal for very low velocities, where in the back-scattering configuration no oscillations would be observed. The extent of the overlap volume in the gradient direction of the two lasers is about $100\,\mu$m, which determines the spatial resolution for the determination of the local velocity at the position where the laser beams cross. The lens L1 is mounted on a motorized translation stage (Melles Griot, Nanomotion II), with a resolution of $1\,\mu$m, in order to sweep the focal point through the gap. The lenses L2 and L4 focus the scattered light of the two beams through pinholes onto a PMT. Both PMTs, for the forward and back scattering configuration, are connected to a correlator with a linear time spacing [70].

Typical velocity profiles are depicted in Fig. 3 for the same concentrations 7.4, 11.1, and 14.8 mg/ml as in Fig. 2, well below, just below, and above the glass transition, respectively. These profiles are independent of the history of the samples; they fully develop within a few minutes (contrary to the star-polymer glasses in Ref. [18], where the formation of shear bands takes many hours), and do not change to within experimental error over time spans of several days.

Far below the glass concentration, for shear rates less than about $30\,\mathrm{s}^{-1}$ there is severe slip on both the stationary and moving surfaces of the Couette cell, so that the suspension flows like a plug [see Fig. 3(a)]. For larger shear rates, nonuniform flow profiles are observed, where no slip occurs at the stationary outer cylinder surface, while slip is still significant at the rotating inner cylinder [as indicated by the left-pointing arrows on the right axis in Fig. 3(b)]. There is no shear banding, in the sense that there are no clear separate bands within which the shear rate is independent of position. The inhomogeneous flow profiles for this low concentration are attributed to the natural variation of the shear rate within the gap of the Couette cell in combination with shear thinning [25].

The flow behavior changes in the vicinity of the glass transition [see Figs. 3(c) and 3(d)] and within the glass [see Figs. 3(e) and 3(f)]. Up to shear rates of about 30–$40\,\mathrm{s}^{-1}$, internal fracture is observed for both concentrations [Figs. 3(c) and 3(e)], where there is a jump in the flow velocity within the bulk of the suspensions. The position where fracture occurs is independent of the applied shear rate. The two regions on both sides of the location where fracture occurs have a constant velocity, independent of position, except for the highest applied shear rate where the velocity near the inner cylinder slightly increases [see the upper red data points in Figs. 3(c) and 3(e)]. Hence, plug flow is observed on both sides of the location where internal fracture occurs. There is an appreciable slip at the stationary outer cylinder and essentially no slip at the rotating inner cylinder [as indicated by the left-pointing horizontal arrows in Figs. 3(c) and 3(e)]. Similar slip phenomena (without fracture) have also been observed in hard-sphere glasses on lowering the applied shear rate [71] and for concentrated emulsions [33–35].

As will be discussed below, there is no indication of fracture and slip for small cell gap widths (similar to the domain size), for which the orientational texture is absent. For such small-gap shear cells the stress response of the material within a single domain is probed. The observed fracture and slip in the large-gap shear cell is therefore attributed to the stress response of the orientational chiral-nematic texture, rather than the response of the uniform chiral-nematic phase within single domains. The domain-domain interactions are thus responsible for the brittle nature of the dispersion that leads to fracture. Contrary to concentrations in the vicinity and within the glass, nematic domains are fluid-like for concentrations far below the glass transition, which is most probably the reason that no internal fracture is observed for the low concentration in Fig. 3(a). Note that the mechanism of internal fracture being due to the presence of domains is unique to glasses of rods in the full nematic state: such domains are absent in glasses of spherical particles.

Above a shear rate of about $40\,\mathrm{s}^{-1}$ the combined plug-flow and fractured velocity profiles turn into a gradient-banded flow [see Figs. 3(d) and 3(f)]. The gradient bands are more pronounced for the concentration within the glass. For shear rates larger than $150\,\mathrm{s}^{-1}$, the velocity profile along the gradient direction becomes linear. In the case the vorticity bands exhibit internal rolling flow [as sketched in Fig. 3(h)], which is expected for any of the vorticity-banding scenarios discussed in the previous section, the gradient banded flow is superimposed onto the vorticity rolling flow. The rolling flow velocity within the bands is very much weaker as compared to the applied shear flow [59]. The possible rolling flow is apparently too weak to significantly blur the flow profile in the gradient direction. A sketch of the various shear-rate regimes where different types of inhomogeneous flows are observed for the higher concentrations is given in Fig. 3(g). Note that vorticity banding sets in at shear rates somewhat below the shear rate where gradient-banding occurs.

One may ask why shear banding takes over from fracture and plug flow at higher shear rates. It turns out that the domain-texture morphology at these higher shear rates changes considerably (as seen from the images in Fig. 2). The change in the domain morphology affects the interactions between the domains, and therefore the tendency to fracture. How the changes in the texture morphology affects the tendency to fracture is an open question that is beyond the scope of the present study. The shear thinning due to small-scale structure deformation of the material within single domains that leads to banding (as will be shown below) requires higher shear rates as compared to the shear rates where the large-scale texture morphology is distorted.
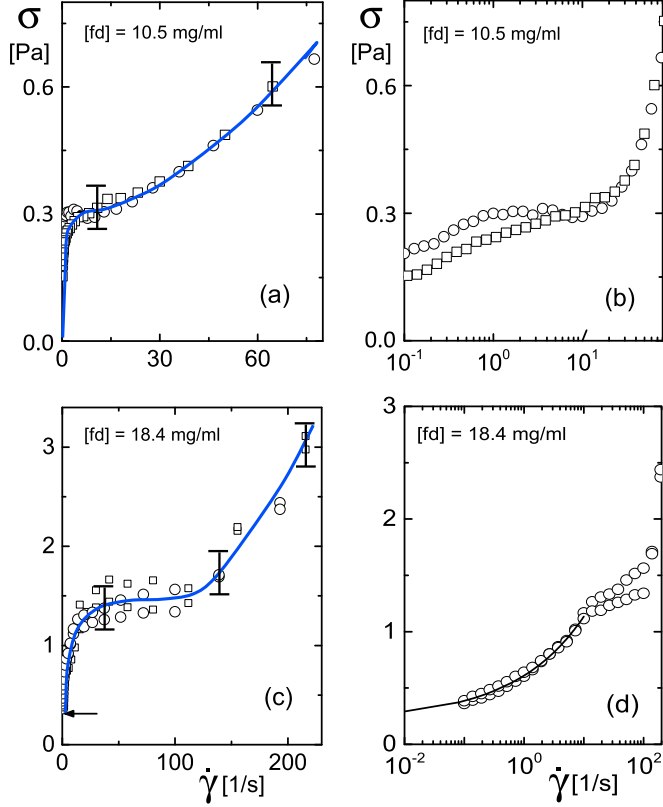
FIG. 4. (a), (b) Flow curves for a fd-concentration of 10.5 mg/ml just below the glass transition, on a linear shear-rate scale (a) and a logarithmic scale (b). The plots in (b) emphasize the low shear rate behavior of the stress. (c), (d) The same as for (a), (b), but now for a concentration of 18.4 mg/ml well within the glass. The solid curve in (d) is a Herschel-Bulkley fit within the low shear rate regime, with an exponent of 0.37 ± 0.07 and a yield stress of 0.22 ± 0.03 Pa, which is indicated by the arrow in (c). Circles and squares represent sweeps with increasing and decreasing shear rate, respectively. The blue lines are drawn to guide the eye.

To asses the complex flow behavior resulting from the rheological response of the uniform chiral-nematic phase within single domains, rheological data have been obtained with a small-gap cone-plate shear cell with linear dimensions similar to those of single chiral-nematic domains. The chiral-nematic domain size is 100–300 μm, while the maximum gap width of the cone-plate geometry, at the outer rim of the cell, is 400 μm. Therefore, the measured shear stress in the experiments discussed below essentially relates to the stress response of the homogeneous chiral-nematic phase within a single domain. We use a sensitive strain-controlled rheometer ARES 100 FRTN1 with a cone-plate geometry. The cone radius is 12.5 mm, and the cone angle is 0.04 radians. The cone and plate are made of stainless steel with smooth walls. Directly after loading the sample, the shear rate is kept at $100\,\text{s}^{-1}$ for 20 s. Subsequently, the shear rate is lowered stepwise to record the stress during 20 s for each data point, down to a shear rate of $0.1\,\text{s}^{-1}$. The same protocol is then applied upon subsequent stepwise increasing the shear rate.

Flow curves as measured with the small-gap geometry for two concentrations, just below and above the glass transition, are shown in Fig. 4. The flow curve for the concentration of 10.5 mg/ml just below the glass transition are given in Figs. 4(a) and 4(b), and for a concentration well within the glass in Figs. 4(c) and 4(d), both with a linear and logarithmic shear-rate scale. The experimental error in the concentration is about 0.6 mg/ml, so that the concentration of 10.5 mg/ml is essentially the same as the concentration of 11.1 mg/ml in Figs. 2 and 3. Figures 4(b) and 4(d) with a logarithmic

shear-rate scale emphasize the behavior at small shear rates. The open circles and squares represent data points during sweeps with increasing and decreasing shear rate, respectively. There is some hysteresis for the downward and upward sweeps, in the sense that the measured stresses during a downward and upward sweep differ. This observation is attributed to the time required for the gradient-banded velocity profiles to relax and to reform at these low shear rates. Keeping the shear rate constant for several hundreds of seconds at a given value during a downward sweep indeed reveals a change of the stress towards its value found during the upward sweep. As can be seen from Fig. 4, there is a stress plateau just below the glass transition, while the stress plateau is quite pronounced within the glass. Flow curves for fd-virus suspensions as reported in Ref. [69] within the full nematic state, but far below the glassy state, are monotonically increasing (see in particular their Fig. 3: multiplying the viscosity in that figure by the shear rate shows that the stress is monotonically increasing with shear rate, without indications for a stress plateau). As discussed below, stress plateaus are indicative for gradient banding, in accordance with the observed flow profiles for the two higher concentrations in Fig. 3. Since the flow curves refer to the rheological response of the uniform chiral-nematic material within domains, the banded velocity profiles are attributed to the response of single domains.

The fractured flow profiles in Fig. 3 are attributed to domain-domain interactions, which are absent in the small-gap cell used to obtain the flow curves in Fig. 4. In the vicinity of the glass transition and within the glass, the domains act as elastic objects, which tend to assembly in layers under flow conditions (similar to the layers formed in flowing crystalline hard sphere suspensions [72,73]). The flow-induced tendency to assembly in layers might be at the origin of fracture. The spacing between the adjacent sliding layers that constitute the fractured region is filled with solvent having a relatively low viscosity, which would lead to a quasiplateau of the stress at small shear rates (lower than about 30–$40\,s^{-1}$). Such a stress plateau at these small shear rates is not observed when the gap in the measurement geometry encompasses virtually only one domain, as is the case of the flow curves in Fig. 4, obtained via rheometric measurements (as discussed above). This suggests that fracture as seen in Fig. 3 is indeed due to domain-domain interactions. That fracture is accompanied by a virtual stress plateau is experimentally observed for other types of systems. The measured stress of Laponite dispersions [74] and bridged microemulsions [75] decreases with increasing shear rate in the stationary state when fracture occurs. A quasistress plateau upon fracturing of wormlike micelles has been observed in Ref. [76] (although fracture is accompanied by another instability) and in transient networks of surfactant micelles linked by block copolymers [77]. Overviews of fracture and slip of complex fluids can be found in Refs. [78,79]. The investigation of the precise nature of the fractured region in our rod system is outside the scope of the present study.

A stress plateau at intermediate shear rates is found for various types of systems that exhibit the "classic gradient-banding instability," such as wormlike micellar solutions, lyotropic lamellar phases, solutions and blends of various types of polymers, polycrystalline colloids, and dispersions of platelets [10–16,22–26]. This instability is due to very strong shear thinning, such that the stress of the *homogeneously sheared system*, before banding sets in, decreases with increasing shear rate within a certain shear-rate regime leading to an effectively negative viscosity. In the *fully gradient-banded, stationary state* where two regions (the "bands") of high and low shear rate coexist, the stress is strictly independent of the applied shear rate, although the stress plateau may be slightly tilted in case there is coupling to concentration [12,80]. In a controlled shear-rate experiment, the flow curve in the stationary state (where bands are fully developed) therefore exhibits a stress plateau. The stress is constant in the same intermediate shear-rate range where banding occurs, as observed in Fig. 4 for the two highest concentrations. The stress plateau that we find in the small-gap shear cell thus implies that the chiral-nematic material within single domains shear-thins to a sufficient extent to give rise to the classic banding instability, in accordance with the banded flow profiles that are seen in Fig. 3. This type of instability has also been observed in soft-sphere glasses of star polymers [20,21]. The microscopic origin of strong shear-thinning behavior in various systems can be quite different. Unlike glasses of spherical colloids, the shear thinning of suspensions of

very long and thin rodlike particles is due to shear-induced alignment of the rods. A stress plateau in combination with the similar hysteresis effects as discussed above have also been found in glasses of starlike polymers [17–19,81] and in emulsions filled with 40% of colloidal particles [82].

IV. SOFT GLASSES VERSUS HARD GLASSES

In this section, we argue that the gradient-banding scenario of glasses of colloids with long-ranged repulsive interactions ("soft glasses") can be fundamentally different from glasses of particles with short-ranged repulsive interactions ("hard glasses"). We also provide a brief overview of the banding behavior of various other types of colloidal glasses.

There is a second type of shear-banding instability that is fundamentally different from the classic shear-banding scenario, where gradient-banded flow is the result of particle transport induced by spatial gradients in the shear rate [16,37,38,83,84], the so-called Shear-gradient Concentration Coupling (SCC) instability. This instability is found experimentally for colloidal hard-sphere glasses in Ref. [37], and a microscopic theory is developed in Ref. [38] for shear-gradient induced mass transport of spherical colloids which is indeed shown to lead to gradient banding in hard-sphere glasses. The origin of the SCC instability can be understood intuitively as follows. Due to an increased concentration of colloids in part of the shear cell (typically close to one of the shear-cell walls), as a result of shear-gradient–induced mass transport, the local yield stress becomes larger than the actual stress, giving rise to a region (one of the "bands") where the suspension does not flow. Such a banded state occurs for sufficiently small shear rates. Contrary to the classic gradient-banding instability, the stress monotonically increases with increasing shear rate so that no stress plateau in the flow curve is observed. The SCC instability leads to banded flows in colloidal glasses of hard spheres [37–39]. The SCC instability requires a yield stress that is a strong increasing function with concentration, since in that case the increased concentration due to shear-gradient induced mass transport gives rise to a significant increase of the local yield stress. Such a strong concentration-dependent yield stress is found for glasses of colloids with short-ranged repulsive interactions, due to the strongly reduced free volume on approach of the maximum packing fraction where the yield stress diverges. The concentration dependence of the yield stress of hard-sphere glasses, for example, diverges on approach of the maximum random packing fraction $\varphi_m = 0.64$ as $\sim (\varphi_m - \varphi)^{-3}$ (with φ the volume fraction) due to the vanishing free volume that is available for a sphere [37].

There may be a gradual transition from the classic banding transition to the SCC instability. The classic banding transition may occur transiently, after which much slower gradient-induced mass transport takes over, leading subsequently to the SCC instability.

For glasses of soft colloids, the concentration dependence of the yield stress is much weaker as compared to glasses of hard spheres, so that the SCC instability will not occur. Such a relatively weak concentration dependence of the yield stress for our soft rod-glass up to quite large concentrations (of about four times the glass-transition concentration) is evident from Fig. 5(a). Here the blue data points are obtained from dynamic strain sweeps and the red data points from transient shear measurements [85]. The origin of the left axis in Fig. 5(a) corresponds to the glass-transition concentration ($c_g = 11.7 \pm 0.5$ mg/ml). Note that due to the small amount of sample available, the torque signal was low, and this resulted in relatively large experimental errors. The emerging picture is, however, unambiguous. To within these errors, the yield stress depends on the fd-concentration c through a power-law dependence $\sigma_y/\sigma_y^0 = (c/c_g)^2$ (with σ_y^0 the yield stress at the glass-transition concentration), within the range of concentrations investigated. For some star-polymer systems the yield stress varies linearly with concentration [87].

The complete flow curve consists of a Herschel-Bulkley (HB) shear-rate regime at small shear rates, which gives rise to a quasistress plateau as the stress attains the finite yield stress on lowering the shear rate. In this regime, the stress increases in a power-like fashion with the shear rate. This is clearly shown in Figs. 4(d) and 5(b) (whose captions include details of the HB fitting). A less pronounced increase of the stress with increasing shear rate beyond the Herschel-Bulkley regime is due to the
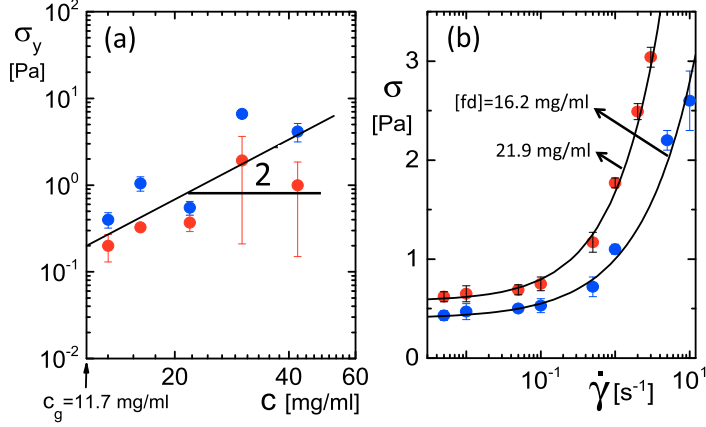
FIG. 5. (a): The concentration dependence of the yield stress σ_y, obtained from the dynamic strain sweeps (blue points) and transient experiments (red circles). We note that, in the range of strains covered (0.5%–500% at 1 rad/s), there is no evidence of two-step yielding [86]. The line through the data points has a slope of 2 (see text). The origin of the vertical axis corresponds to the glass transition concentration $c_g = 11.7$ mg/ml. (b) Stress versus shear rate obtained from transient step-rate tests (see text). Blue and red data points correspond to fd-glass concentrations of 16.2 mg/ml and 21.9 mg/ml, respectively. The solid lines are fits to the empirical Herschel-Bulkley model. For the lowest concentration it is found that $\sigma_y = (0.40 \pm 0.05)$ Pa and $\nu = 0.6 \pm 0.1$, while for higher concentration $\sigma_y = (0.58 \pm 0.10)$ Pa and $\nu = (0.7 \pm 0.1)$.

onset of shear thinning that ultimately leads to shear banding, as evidenced by a stress plateau at intermediate shear rates. At even higher shear rates the stress increases again when banding ceases to occur.

Figure 4(d) shows that the Herschel-Bulkley type of behavior indeed becomes invalid beyond shear rates where strong shear thinning gives rise to gradient banding. We therefore limited the Herschel-Bulkley fits in Fig. 5(b) to shear rates below $10\,\mathrm{s}^{-1}$. After a preshear period of $100\,\mathrm{s}$ at a shear rate of $10\,\mathrm{s}^{-1}$, the samples were left to relax without shearing for about $400\,\mathrm{s}$. Each data point in Fig. 5(b) was obtained by a step jump to the desired shear rate, after which the stress was determined from the time-independent stress plateau. The solid curves in Fig. 5(b) are fits to the empirical Herschel-Bulkley model, $\sigma(\dot{\gamma}) = \sigma_y + K\,\dot{\gamma}^{\nu}$, where σ_y is the yield stress, K is a constant (with dimension $\mathrm{Pa\,s}^{\nu}$), and the exponent ν describes shear thinning for stress values above yielding. The exponent for our Wigner rod-glass is found to be slightly larger than the value of 0.5 for colloidal glasses of both soft spheres [88–91] and hard spheres [7,37] and increases with concentration. This is a nontrivial result, as rod alignment plays a crucial role in the shear-thinning mechanism of colloidal rods. The stresses at the relatively higher shear rates are quite a bit larger than the stress plateau in Fig. 4(d). Due to the very long time needed for bands to develop and decay, as discussed earlier, the data in Fig. 5(b) thus most probably relate to the homogeneously sheared system, before banding occurred. The much lower value 0.37 ± 0.07 of the exponent found for the exponent in Fig. 4(d) is therefore due to the onset of shear banding, which leads to an appreciable decrease of the stress. The nonlinear rheology of glassy rodlike colloids exhibits distinct features that underline the importance of shape and make a possible approach towards a universal description most probably unfeasible.

The value of the yield stress at the glass transition of our colloidal rods with long-ranged, soft repulsive interactions is very similar to that of soft spherical colloids [88,89], and significantly smaller than for hard-sphere glasses [7,37,92–94]. These relatively small values of the yield stress of soft-sphere glasses, as well as flow curves with uniform velocity profiles, have been successfully predicted by mode-coupling theory [84,95–99], while for rod-glasses under flow condition there is so far no similar theoretical approach. The respective yield strains for the rod-glass are similar to those of soft and hard spheres [7,90,96,100] and slightly nonspherical colloids with short-ranged

interactions [4–6] (about 10%); however, unlike the sphere-glass [92], they appear to be quite weakly concentration dependent for the rod-glass in the concentration range investigated [101].

The shear-banding behavior and rheology of soft colloidal particles may be affected by additional features concerning their interactions. The flow of highly concentrated suspensions of microgel particles is strongly affected by their elastic deformability, while for star polymers there is the additional possibility of mutual interpenetration [102]. Glasses of microgel particles at quite high packing fractions do not exhibit shear-banded flows [103,104]. These systems do not very strongly shear-thin (to give rise to the classic banding instability), and the yield stress does not increase sufficiently strongly with increasing concentration (to exhibit an SCC instability). The reason for the latter can be understood as being the result of elastic deformability of the microgel particles, which diminishes the increase of the yield stress with increasing concentration resulting from the loss of free volume as compared to undeformable hard-spheres. The elastohydrodynamic model in Refs. [103,105] quantitatively describes the effect of elasticity on the flow behavior of microgel particles. Star polymers are expected to exhibit the classic shear-banding instability due to transient forces arising from interpenetrating arms [21,105–109]. The classic banding scenario is indeed observed for star-polymer glasses, although the link between arm disengagement and strong shear thinning is not directly evident. Hence the entire mechanism is not yet completely understood [17–21,81].

V. DISCUSSION AND CONCLUSIONS

We have shown that glasses of colloidal rods exhibit uniquely heterogeneous flow behavior due to the dynamic arrest of chiral-nematic orientational textures and their constituent rods. The presence of two length scales (rod-cage size and domain size), which can be probed by appropriate selection of the gap width of the shear cell in the flow experiments, is unique for one-component colloids suspended in solvent and is at the origin of the unprecedented flow properties of rod-glasses. They involve three distinct signatures: (1) internal fracture, due to domain-domain interactions, as well as plug flow with slip at low shear rates, (2) gradient-banded flow due to the strong thinning of the uniform chiral-nematic phase within single domains at intermediate shear rates, and (3) eventually uniform flow at high shear rates. The observed shear banding complies with the classic gradient-banding scenario that gives rise to a stress plateau in the flow curve. Whereas this scenario is generic and does not necessary involve glasses, here it has been evidenced for these soft glasses with a weak low-shear rate stress plateau.

Remarkably, glasses of spherical colloids do not exhibit plug flow and fracture whereas they do exhibit gradient-banded flow profiles. With the support of the present results there are now strong indications that the origin of the gradient-banded flow is fundamentally different for glasses consisting of particles with soft, long-ranged interactions (such as the fd-virus rods), as compared to their counterparts with hard, short-ranged repulsive interactions. For glasses of colloids with long-ranged interactions, shear banding is due to the classic banding scenario that requires strong shear thinning of the homogeneously sheared system. It is associated with a significant stress plateau region at intermediate shear rates and may or may not exhibit yield stress, depending on whether the system is glassy (as here) or not. On the other hand, hard-sphere glasses exhibit the shear-gradient concentration coupling (SCC) instability, which is a consequence of shear-gradient induced mass transport. In that case, a yield stress represents a distinct feature at low shear rates, followed by weak thinning at higher rates, beyond banding.

There are both differences and similarities in the rheological behavior of glasses of rods and of spheres. The shear thinning behavior well within the colloidal-rod glassy state at low shear rates (below shear rates where banding occurs) is found to follow a Herschel-Bulkley dependence, with the so-determined yield stress signifying the glass, with a higher thinning exponent as compared to glasses of spheres, which increases with concentration. Moreover, the yield stress at the glass transition for soft-sphere and soft-rod glasses is remarkably similar, yet significantly smaller than that of hard-sphere glasses and has a much weaker concentration dependence. Finally, a universal yield strain of the order of 10% appears to emerge, being virtually independent of concentration.

These general features reflect the fundamental differences between the rheology and in particular the mechanisms leading to shear banding of soft and hard colloidal glasses. The present results open the door for exploring shape as a lead parameter in the design and use of soft colloidal composites.

There are several outstanding challenges, both experimental and theoretical, resulting from this work. The origin of fracture in rod-glasses as compared to other types of systems [74–76], as well as the nature of the transition between fracture and plug flow to a banded flow profile are subjects for future research. The question whether this is a sharp transition, or there exist complex flow profiles where fracture, plug flow, and banding are combined within a certain shear-rate interval, requires accurate flow-profile experiments with very small incremental steps in the applied shear rate. It is a challenge to predict fracture and plug flow from a description of the shear-affected orientational texture in combination with the elasticity of domains. It would be interesting to connect the microscopic approach of the stationary gradient-banded state due to the SCC instability in Ref. [38] with the empirical fluidity model. In describing the classic- and SCC gradient-banding transitions it is essential to account for nonlocal stresses. As yet there is no microscopic theory that allows to predict such stresses from interparticle potentials. Finally, exploring the occurrence of transient banding and the possibility of a smooth transition between the classic and SCC instability offer exciting opportunities for further investigations.

---

[1] M. J. Solomon and P. T. Spicer, Microstructural regimes of colloidal rod suspensions, gels, and glasses, Soft Matter **6**, 1391 (2010).

[2] E. Zaccarelli and W. C. K. Poon, Colloidal glasses and gels: The interplay of bonding and caging, Proc. Natl. Acad. Sci. USA **106**, 15203 (2009).

[3] G. J. Hunter and E. R. Weeks, The physics of the colloidal glass transition, Rep. Prog. Phys. **75**, 066501 (2012).

[4] R. C. Kramb and C. F. Zukoski, Nonlinear rheology and yielding in dense suspensions of hard anisotropic colloids, J. Rheol. **55**, 1069 (2011).

[5] R. C. Kramb and C. F. Zukoski, Yielding in dense suspensions: Cage, bond, and rotational confinements, J. Phys: Condens. Matter **23**, 035102 (2011).

[6] R. C. Kramb, R. Zhang, K. S. Schweizer, and C. F. Zukoski, Re-entrant kinetic arrest and elasticity of concentrated suspensions of spherical and nonspherical repulsive and attractive colloids, J. Chem. Phys. **134**, 014503 (2011).

[7] K. N. Pham, G. Petekidis, D. Vlassopoulos, S. U. Egelhaaf, W. C. K. Poon, and P. N. Pusey, Yielding behavior of repulsion- and attraction-dominated colloidal glasses, J. Rheol. **52**, 649 (2008).

[8] Z. Zhou, J. V. Hollingsworth, S. Hong, H. Cheng, and C. C. Han, Yielding behavior in colloidal glasses: Comparison between hard cage and soft cage, Langmuir **30**, 5739 (2014).

[9] M. E. Helgeson, N. J. Wagner, and D. Vlassopoulos, Viscoelasticity and shear melting of colloidal star polymer glasses, J. Rheol. **51**, 297 (2007).

[10] S. M. Fielding, Complex dynamics of shear banded flows, Soft Matter **3**, 1262 (2007).

[11] P. T. Callaghan, Rheo NMR and shear banding, Rheol. Acta **47**, 243 (2008).

[12] J. K. G. Dhont and W. J. Briels, Gradient and vorticity banding, Rheol. Acta **47**, 257 (2008).

[13] P. D. Olmsted, Perspectives on shear banding in complex fluids, Rheol. Acta **47**, 283 (2008).

[14] S. Manneville, Recent experimental probes of shear banding, Rheol. Acta **47**, 301 (2008).

[15] T. Divoux, M. A. Fardin, S. Manneville, and S. Lerouge, Shear banding of complex fluids, Ann. Rev. Fluid Mech. **48**, 81 (2016).

[16] J. K. G. Dhont, K. Kang, M. P. Lettinga, and W. J. Briels, Shear banding instabilities, Kor.-Austral. Rheol. J. **22**, 291 (2010).

[17] W. M. Holmes, P. T. Callaghan, D. Vlassopoulos, and J. Roovers, Shear banding phenomena in ultrasoft colloidal glasses, J. Rheol. **48**, 1085 (2004).

[18] S. A. Rogers, D. Vlassopoulos, and P. T. Callaghan, Aging, Yielding, and Shear Banding in Soft Colloidal Glasses, Phys. Rev. Lett. **100**, 128304 (2008).

[19] A. N. Beris, E. Stiakakis, and D. Vlassopoulos, A thermodynamically consistent model for the thixotropic behavior of concentrated star polymer solutions, J. Non-Newtonian Fluid Mech. **152**, 76 (2008).

[20] S. A. Rogers, P. T. Callaghan, G. Petekidis, and D. Vlassopoulos, Time-dependent rheology of colloidal star glasses, J. Rheol. **54**, 133 (2010).

[21] W. J. Briels, D. Vlassopoulos, K. Kang, and J. K. G. Dhont, Constitutive equations for the flow behavior of entangled polymeric systems: Application to star polymers, J. Chem. Phys. **134**, 124901 (2011).

[22] P. D. Olmsted and C.-Y. D. Lu, Phase coexistence of complex fluids in shear flow, Faraday Discuss. **112**, 183 (1999).

[23] J. K. G. Dhont, A constitutive relation describing the shear-banding transition, Phys. Rev. E **60**, 4534 (1999).

[24] C.-Y. D. Lu, P. D. Olmsted, and R. C. Ball, Effects of Nonlocal Stress on the Determination of Shear Banding Flow, Phys. Rev. Lett. **84**, 642 (2000).

[25] J.-B. Salmon, S. Manneville, and A. Colin, Shear banding in a lyotropic lamellar phase. I. Time-averaged velocity profiles, Phys. Rev. E **68**, 051503 (2003).

[26] P. Coussot and G. Ovarlez, Physical origin of shear-banding in jammed systems, Eur. Phys. J. E **33**, 183 (2010).

[27] P. Sollich, F. Lequeux, P. Hebraud, and M. E. Cates, Rheology of Soft Glassy Materials, Phys. Rev. Lett. **78**, 2020 (1997).

[28] P. Sollich, Rheological constitutive equation for a model of soft glassy materials, Phys. Rev. E **58**, 738 (1998).

[29] S. M. Fielding, M. E. Cates, and P. Sollich, Shear banding, aging and noise dynamics in soft glassy materials, Soft Matter **5**, 2378 (2009).

[30] P. C. F. Moller, S. Rodts, M. A. J. Michels, and D. Bonn, Shear banding and yield stress in soft glassy materials, Phys. Rev. E **77**, 041507 (2008).

[31] A. Fall, J. Paredes, and D. Bonn, Yielding and Shear Banding in Soft Glassy Materials, Phys. Rev. Lett. **105**, 225502 (2010).

[32] S. Jarny, N. Roussel, S. Rodts, F. Bertrand, R. Le Roy, and P. Coussot, Rheological behavior of cement pastes from MRI velocimetry, Cement Concrete Res. **35**, 1873 (2005).

[33] L. Becu, S. Manneville, and A. Colin, Yielding and Flow in Adhesive and Nonadhesive Concentrated Emulsions, Phys. Rev. Lett. **96**, 138302 (2006).

[34] A. Ragouilliaux, G. Overlaz, N. Shahidzadeh-Bonn, B. Herzhaft, T. Palermo, and P. Coussot, Transition from a simple yield-stress fluid to a thixotropic material, Phys. Rev. E **76**, 051408 (2007).

[35] A. Y. Malkin and V. G. Kulichikhin, Structure and rheology of highly concentrated emulsions: A modern look, Russ. Chem. Rev. **84**, 803 (2015).

[36] G. Ovarlez, S. Rodts, X. Chateau, and P. Coussot, Phenomenology and physical origin of shear-localization and shear-banding in complex fluids, Rheol. Acta **48**, 831 (2009).

[37] R. Besseling, L. Isa, P. Ballesta, G. Petekidis, M. E. Cates, and W. C. K. Poon, Shear Banding and Flow-Concentration Coupling in Colloidal Glasses, Phys. Rev. Lett. **105**, 268301 (2010).

[38] H. Jin, K. Kang, K.-H. Ahn, and J. K. G. Dhont, Flow instability due to coupling of shear-gradients with concentration: Non-uniform flow of (hard-sphere) glasses, Soft Matter **10**, 9470 (2014).

[39] F. Varnik, L. Bocquet, J.-L. Barrat, and L. Berthier, Shear Localization in a Model Glass, Phys. Rev. Lett. **90**, 095702 (2003).

[40] A. Wierenga, A. P. Philipse, and H. N. W. Lekkerkerker, Aqueous dispersions of colloidal Boehmite: Structure, dynamics, and yield stress of rod gels, Langmuir **14**, 55 (1998).

[41] K. Kang and J. K. G. Dhont, Glass Transition in Suspensions of Charged Rods: Structural Arrest and Texture Dynamics, Phys. Rev. Lett. **110**, 015901 (2013).

[42] K. Kang and J. K. G. Dhont, Structural arrest and texture dynamics in suspensions of charged colloidal rods, Soft Matter **9**, 4401 (2013).

[43] S. Fraden, Phase transitions in colloidal suspensions of virus particles, in *Observation, Prediction and Simulation of Phase Transitions in Complex Fluids*, edited by M. Baus, L. F. Rull, and J. P. Ryckaert, NATO-ASI-Series C 460 (Kluwer Academic Publishers, Dordrecht, 1995), 113.

[44] Z. Dogic and S. Fraden, Cholesteric phase in virus suspensions, Langmuir **16**, 7820 (2000).

[45] Z. Dogic and S. Fraden, Development of model colloidal liquid crystals and the kinetics of the isotropic-smectic transition, Phil. Trans. R. Soc. Lond. A Math. Phys. Eng. Sci. **359**, 997 (2001).

[46] E. Grelet and S. Fraden, What is the Origin of Chirality in the Cholesteric Phase of Virus Suspensions? Phys. Rev. Lett. **90**, 198302 (2003).

[47] Z. Dogic and S. Fraden, Phase behavior of rod-like viruses and virus-sphere mixtures, in *Soft Matter*, Vol. 2, Complex Colloidal Suspensions, edited by G. Gompper and M. Schick (Wiley-VCH Verlag, Weinheim, 2006).

[48] E. Grelet and R. Rana, From soft to hard rod behavior in liquid crystalline suspensions of sterically stabilized colloidal filamentous particles, Soft Matter **12**, 4621 (2016).

[49] E. Wigner, Effects of the electron interaction on the energy levels of electrons in metals, Trans. Farad. Soc. **34**, 678 (1938).

[50] F. Huang, R. Rotstein, S. Fraden, K. E. Kasza, and N. T. Flynn, Phase behavior and rheology of attractive rod-like particles, Soft Matter **5**, 2766 (2009).

[51] Z. Zhang, N. Krishna, M. P. Lettinga, J. Vermant, and E. Grelet, Reversible gelation of rod-like viruses grafted with thermoresponsive polymers, Langmuir **25**, 2437 (2009).

[52] G. I. Taylor, Stability of a viscous liquid contained between two rotating cylinders, Phil. Trans. R. Soc. London A **223**, 289 (1923).

[53] R. G. Larson, Instabilities in viscoelastic flows, Rheol. Acta **31**, 213 (1992).

[54] M. A. Fardin, T. J. Ober, C. Gay, G. Grégoire, G. H. McKinley, and S. Lerouge, Criterion for purely elastic Taylor-Couette instability in the flows of shear-banding fluids, Europhys. Lett. **96**, 44004 (2011).

[55] S. M. Fielding, Viscoelastic Viscoelastic Taylor-Couette Instability of Shear Banded Flow, Phys. Rev. Lett. **104**, 198303 (2010).

[56] K. Kang, M. P. Lettinga, Z. Dogic, and J. K. G. Dhont, Vorticity banding in rodlike virus suspensions, Phys. Rev. E **74**, 026307 (2006).

[57] K. Kang, M. P. Lettinga, and J. K. G. Dhont, Is vorticity-banding due to an elastic instability? Rheol. Acta. **47**, 499 (2008).

[58] S. M. Fielding, Vorticity structuring and velocity rolls triggered by gradient shear bands, Phys. Rev. E **76**, 016311 (2007).

[59] See Supplemental Material at http://link.aps.org/supplemental/10.1103/PhysRevFluids.2.043301 for videos of the sheared suspensions, in Sec. I.

[60] E. Marsano, L. Carpaneto, A. Ciferri, and Y. Wu, Formation of a banded texture in solutions of liquid-crystalline polymers 11. poly(n-hexylisocyanate) in toluene, Liquid Crystals **3**, 1561 (1988).

[61] P. L. Maffetone, N. Grizzuti, and G. Marrucci, Band formation in HPC solutions by consecutive shears along orthogonal directions, Liquid Crystals **4**, 385 (1989).

[62] B. Ernst and P. Navard, Band textures in mesomorphic (hydroxypropyl) cellulose solutions, Macromolecules **22**, 1419 (1989).

[63] J. T. Gleeson, R. G. Larson, D. W. Mead, G. Kiss, and P. E. Cladis, Image analysis of shear-induced textures in liquid-crystalline polymers, Liquid Crystals **11**, 341 (1992).

[64] S. J. Picken, P. Moldenaers, S. Berghmann, and J. Mewis, Experimental and theoretical analysis of band formation in polymeric liquid crystals upon cessation of flow, Macromolecules **25**, 4759 (1992).

[65] T. De'Neve, P. Navard, and M. Kléman, Shear rheology and shear-induced textures of a thermotropic copolyesteramide, J. Rheol. **37**, 515 (1993).

[66] R. G. Larson and D. W. Mead, The ericksen number and deborah number cascades in sheared polymeric nematics, Liquid Crystals **15**, 151 (1993).

[67] J. Vermant, P. Moldenaers, J. Mewis, and S. J. Picken, Band formation upon cessation of flow in liquid-crystalline polymers, J. Rheol. **38**, 1571 (1994),

[68] J. Vermant, P. Moldenaers, S. J. Picken, and J. Mewis, A comparison between texture and rheological behavior of lyotropic liquid crystalline polymers during flow, J. Non-Newt. Fluid Mech. **53**, 1 (1994).

[69] M. P. Lettinga, Z. Dogic, H. Wang, and J. Vermant, Flow behavior of colloidal rodlike viruses in the nematic phase, Langmuir **21**, 8048 (2005).

[70] See Supplemental Material at http://link.aps.org/supplemental/10.1103/PhysRevFluids.2.043301 for typical examples of correlations functions and their fits, in Sec. I.

[71] P. Ballesta, R. Besseling, L. Isa, G. Petekidis, and W. C. K. Poon, Slip and Flow of Hard-Sphere Colloidal Glasses, Phys. Rev. Lett. **101**, 258301 (2008).

[72] D. Derks, H. Wisman, A. van Blaaderen, and A. Imhof, Confocal microscopy of colloidal dispersions in shear flow using a counter-rotating cone-plate shear cell, J. Phys.: Condens. Matter **16**, 3917 (2004).

[73] D. Derks, Y. L. Wu, A. van Blaaderen, and A. Imhof, Dynamics of colloidal crystals in shear flow, Soft Matter **5**, 1060 (2009).

[74] F. Pignon, A. Magnin, and J.-M. Piau, Thixotropic colloidal suspensions and flow curves with a minimum: Identification of flow regimes and rheometric consequences, J. Rheol. **40**, 573 (1996).

[75] H. Tabuteau, S. Mora, G. Porte, M. Abkarian, and C. Ligoure, Microscopic Mechanism of the Brittleness of Viscoelastic Fluids, Phys. Rev. Lett. **102**, 155501 (2009).

[76] Y. T. Hu, P. Boltenhagen, E. Matthys, and D. J. Pine, Shear thickening in low-concentration solutions of wormlike micelles. II. Slip, fracture, and stability of the shear-induced phase, J. Rheol. **42**, 1209 (1998).

[77] L. Ramos A. Laperrousaz, P. Dieudonné, and C. Ligoure, Structural Signature of a Brittle-to-Ductile Transition in Self-Assembled Networks, Phys. Rev. Lett. **107**, 148302 (2011).

[78] C. Ligoure and S. Mora, Fractures in complex fluids: The case of transient networks, Rheol. Acta **52**, 91 (2013).

[79] M. Cloitre and R. T. Bonnecaze, A review on wall slip in high solid dispersions, Rheol. Acta, **56**, 283 (2017).

[80] S. M. Fielding and P. D. Olmsted, Flow phase diagrams for concentration-coupled shear banding, Eur. Phys. J. E **11**, 65 (2003).

[81] B. M. Erwin, D. Vlassopoulos, and M. Cloitre, Rheological fingerprinting of an aging colloidal glass, J. Rheol. **54**, 915 (2010).

[82] G. Ovarlez, F. Mahaut, S. Deboeuf, N. Lenoir, S. Hormozi, and X. Chateau, Flows of suspensions of particles in yield stress fluids, J. Rheol. **59**, 1449 (2015).

[83] P. Nozieres and D. Quemada, A possible instability mechanism for plug flow formation in a sheared suspension flow, Europhys. Lett. **2**, 129 (1986).

[84] S. Mandal, M. Gross, D. Raabe, and F. Varnik, Heterogeneous Shear in Hard Sphere Glasses, Phys. Rev. Lett. **108**, 098301 (2012).

[85] See Supplemental Material at http://link.aps.org/supplemental/10.1103/PhysRevFluids.2.043301 for a detailed description of the rheological protocols, in Sec. II.

[86] See Supplemental Material at http://link.aps.org/supplemental/10.1103/PhysRevFluids.2.043301 for the experiments where this is shown, in Sec. II.

[87] B. Erwin, M. Cloitre, M. Gauthier, and D. Vlassopoulos, Dynamics and rheology of colloidal star polymers, Soft Matter **6**, 2825 (2010).

[88] M. Cloitre, R. Borrega, F. Monti, and L. Leibler, Glassy Dynamics and Flow Properties of Soft Colloidal Paste, Phys. Rev. Lett. **90**, 068303 (2003).

[89] K. N. Nordstrom, E. Verneuil, P. E. Arratia, A. Basu, Z. Zhang, A. G. Yodh, J. P. Gollub, and D. J. Durian, Microfluidic Rheology of Soft Colloids Above and Below Jamming, Phys. Rev. Lett. **105**, 175701 (2010).

[90] A. Basu, Y. Xu, T. Still, P. E. Arratia, Z. Zhang, K. N. Nordstrom, J. M. Rieser, J. P. Gollub, D. J. Durian, and A. G. Yodh, Rheology of soft colloids across the onset of rigidity: Scaling behavior, thermal, and non-thermal responses, Soft Matter **10**, 3027 (2014).

[91] J. R. Seth, L. Mohan, C. Locatelli-Champagne, M. Cloitre, and R. T. Bonnecaze, A micromechanical model to predict the flow of soft particle glasses, Nat. Mater. **10**, 838 (2011).

[92] A. Le Grand and G. Petekidis, Effects of particle softness on the rheology and yielding of colloidal glasses, Rheol. Acta **47**, 579 (2008).

[93] N. Koumakis, A. Pamvouxoglou, A. S. Poulos, and G. Petekidis, Direct comparison of the rheology of model hard and soft particle glasses, Soft Matter **8**, 4271 (2012).

[94] K. van der Vaart, Y. Rahmani, R. Zargar, Z. Hu, and D. Bonn, Rheology of concentrated soft and hard-sphere suspensions, J. Rheol. **57**, 1195 (2013).

[95] M. Fuchs and M. E. Cates, Theory of Nonlinear Rheology and Yielding of Dense Colloidal Suspensions, Phys. Rev. Lett. **89**, 248304 (2002).

[96] P. Hébraud and F. Lequeux, Mode-Coupling Theory for the Pasty Rheology of Soft Glassy Materials, Phys. Rev. Lett. **81**, 2934 (1998).

[97] J. J. Crassous, M. Siebenbürger, M. Ballauff, M. Drechsler, D. Hajnal, O. Henrich, and M. Fuchs, Shear stresses of colloidal dispersions at the glass transition in equilibrium and in flow, J. Chem. Phys. **128**, 204902 (2008).

[98] M. Siebenbürger, M. Fuchs, and M. Ballauff, Core-shell microgels as model colloids for rheological studies, Soft Matter **8**, 4014 (2012).

[99] C. P. Amann, M. Siebenbürger, M. Ballauff, and M. Fuchs, Nonlinear rheology of glass-forming colloidal dispersions: Transient stress-strain relations from anisotropic mode coupling theory and thermosensitive microgels, J. Phys.: Condens. Matter **27**, 194121 (2015).

[100] N. Koumakis, A. B. Schofield, and G. Petekidis, Effects of shear induced crystallization on the rheology and ageing of hard sphere glasses, Soft Matter **4**, 2008 (2008).

[101] See Supplemental Material at http://link.aps.org/supplemental/10.1103/PhysRevFluids.2.043301 for the corresponding experiments, in Sec. II.

[102] D. Vlassopoulos and M. Cloitre, Tunable rheology of dense soft deformable colloids, Curr. Opinion Coll. Int. Sci. **19**, 561 (2014).

[103] S. P. Meeker, R. T. Bonnecaze, and M. Cloitre, Slip and Flow in Soft Particle Pastes, Phys. Rev. Lett. **92**, 198302 (2004).

[104] J. R. Seth, C. Locatelli-Champagne, F. Monti, R. T. Bonnecaze, and M. Cloitre, How do soft particle glasses yield and flow near solid surfaces? Soft Matter **8**, 140 (2012).

[105] R. T. Bonnecaze and M. Cloitre, Micromechanics of soft particle glasses, Adv. Polym. Sci. **236**, 117 (2010).

[106] A. van den Noort and W. J. Briels, Brownian dynamics simulations of concentration coupled shear banding, J. Non-Newtonian Fluid Mech. **152**, 148 (2008).

[107] W. J. Briels, Transient forces in flowing soft matter, Soft Matter **5**, 4401 (2009).

[108] T. Savin, W. J. Briels, and H. C. Öttinger, Thermodynamic formulation of flowing soft matter with transient forces, Rheol. Acta **52**, 23 (2013).

[109] F. Snijkers, R. Pasquino, P. D. Olmsted, and D. Vlassopoulos, Perspectives on the viscoelasticity and flow behavior of entangled linear and branched polymers, J. Phys.: Condens. Matter **27**, 473002 (2015).